PHYSICAL REVIEW B VOLUME 53, NUMBER 9 1 MARCH 1996-I

Optical second-harmonic generation at interfaces of ferroelectric nanoregions in $SrSiO_3$:Ca

A. Bürgel, W. Kleemann, and U. Bianchi
Angewandte Physik, Gerhard-Mercator-Universität Duisburg, D-47048 Duisburg, Germany

(Received 24 March 1995; revised manuscript received 27 September 1995)

Optical second-harmonic generation (SHG) is observed in $Sr_{1-x}Ca_xTiO_3$ with $x=0.007$ within the ferroelectric domain state below $T_c \approx 18$ K. Surprisingly, its dependence on the polarization angle is incompatible with global C_{2V} symmetry. The appearance of maximum intensity for $\mathbf{E}_\omega \| \mathbf{E}_{2\omega}$ parallel to the nonpolar c axis suggests that SHG is primarily due to symmetry breaking at the interfaces between ferroelectric nanoregions and the paraelectric host material $SrTiO_3$. The observed angular dependences are satisfactorily modeled by assuming the dominant component of the nonlinear surface polarizability to lie parallel to the surface normal of ellipsoidally shaped nanoregions. The unusual electric-field dependence of the SHG intensity recorded at various temperatures and its temporal relaxation after steplike changing the field are described in terms of nanoregion nucleation and condensation in the presence of dipolar random fields.

I. INTRODUCTION

Nonlinear-optical properties of dielectric crystals do not only evidence breaking of inversion symmetry within the bulk of a crystal, but can also arise from structural irregularities.[1,2] These are not necessarily caused by defects, but might also be defined by surfaces and buried interfaces.[3] In this paper we report on second-harmonic generation (SHG) of light, which is very probably due to interfaces of nanoregions, which appear at a random-field (RF) controlled phase transition (PT).

The $Sr_{1-x}Ca_xTiO_3$ (SCT) system is known to undergo a PT into a complex ferroelectric nanoregion state at low temperatures T.[4] The transition temperature depends on the concentration of Ca^{2+} ions, e.g., $T_c \approx 18$ K for $x=0.007$.[4–7] The low-T nanoregion state reveals various types of order on different length scales. Figure 1 shows the schematic nanoregion structure of SCT in its ferroelectric phase with the pseudotetragonal axis $c=z$ and both easy axes $a=x$ and $a'=y$. Ellipsoidally shaped Ca^{2+}-centered polar clusters [so-called[8] ferroelectric microregions (FMR's)], similarly as observed in $K_{1-x}Li_xTaO_3$ (KTL),[9] with strongly increasing size upon cooling to below T_c are assumed to condensate at the percolation threshold and to form ferroelectric domains on a nanometric scale.[6,7] These "nanoregions" are embedded in the paraelectric host lattice of $SrTiO_3$. Furthermore, a striped structure of ferroelectric domains on a micrometric scale develops. The directions of polarization within these domains change between $\pm\mathbf{P}_x$ and $\pm\mathbf{P}_y$ from one ferroelastic domain to another.[4]

When considering SHG within the bulk of ferroelectric domains, one usually anticipates the validity of nonlinear tensor optics. In the present cases of SCT, the SHG tensors referring to $2mm$ and $m2m$ symmetry classes should be applicable.[10] Surprisingly, however, we observe SHG intensities which sharply contradict this principle. Hence a new approach to the interpretation of nonlinear optical effects in SCT is required. Bearing in mind the heterogeneous cluster-like structure depicted in Fig. 1, we propose SHG primarily to be due to the interfaces between the ferroelectric nanoregions and the unperturbed centrosymmetric host material. We thus follow general ideas outlined, e.g., by Shen,[3] who predicts appreciable SHG activity at surfaces and interfaces whenever strong structural or field discontinuities are involved. This applies, e.g., to vicinal surfaces of Si(111), which show appreciable surface SHG efficiency.[11] A preliminary report on the proposed interface SHG mechanism in SCT was given previously.[12]

The paper is organized as follows. In Sec. II we give a brief description of the sample orientations and the experimental setup. Results of measurements with $\mathbf{k}\|x\|[110]_c$ under various polarizations of the fundamental and SH beams and as functions of T and of an external electric field are presented in Sec. III A. Section III B describes and interprets measurements of the SH dynamics upon switching on and off a small external electric field. A model calculation illustrating the interface mechanism of SHG is presented in Sec. IV.

II. EXPERIMENTAL PROCEDURE

The experiments are performed on a SCT crystal with a Ca^{2+} concentration of $x=0.007$. This concentration was obtained by the value of the antiferrodistortive ($O_h \rightarrow D_{4h}$) PT temperature $T_0=125$ K, measured by means of the principal

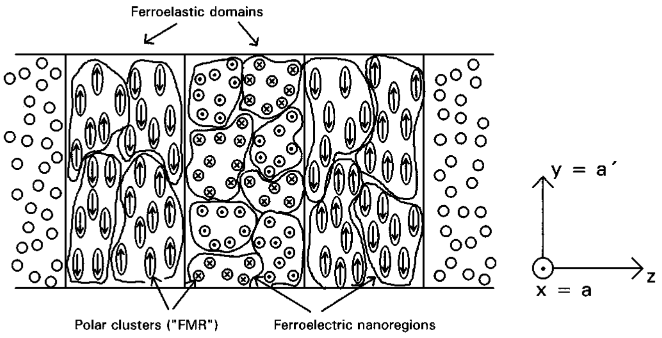

FIG. 1. Schematic view of the ferroelectric low-temperature domain state of $SrTiO_3$:Ca. Ca^{2+}-centered polar clusters [ferroelectric microregions (FMR's)] form ferroelectric nanoregions within ferroelastic domains.

0163-1829/96/53(9)/5222(9)/$10.00 53

birefringence.[4] The sample dimensions are $3.60\times 1.01\times 0.76$ mm^3 along the $[001]_c$ ($\|z$), $[110]_c$ ($\|x$), and $[1\bar{1}0]_c$ ($\|y$) directions, where the index c refers to the cubic phase. Its surfaces are polished to optical quality. The surfaces perpendicular to the y direction are covered with silver paste in order to apply a static external electric field E_y. Temperature-controlled measurements within the range $5\leqslant T\leqslant 300$ K are performed by means of a helium gas-flow cryostat.

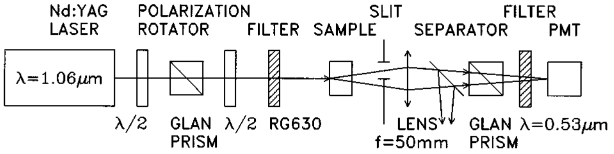

FIG. 2. Experimental setup (schematic). For calibration purposes the sample is replaced by a quartz plate. The movable slit is inserted for measurements of the angular distribution of the SH intensity (see text).

As shown in Fig. 2, the SHG measurements are performed in forward scattering geometry, $\mathbf{k}_{2\omega}\|\mathbf{k}_\omega\|x$ or $\|z$. Hence the field vectors $\mathbf{E}_\omega$ and $\mathbf{E}_{2\omega}$ lie within the (yz) or the (xy) plane, respectively. The pulsed fundamental beam ($\lambda = 1064$ nm) originates from a Q-switched Nd:YAG laser (Baasel Lasertechnik, BLS 600) at a frequency of 1 kHz. The pulse peak powers are about $P\approx 10$ kW with durations $\tau\approx 150$ ns. The polarization of the fundamental beam can be rotated around the direction of propagation by use of a $\lambda/2$-retardation quartz plate of multiple order for high light intensities. SHG contributions originating from the retardation plate are removed by an edge filter, RG 630 (Spindler & Hoyer). The polarization of the divergently diffracted (see below) SH light originating from the SCT sample is collected by a lens, analyzed by a Glan-air polarizer, passing a harmonic separator and an interference filter ($\lambda = 532$ nm), detected by a photomultiplier and processed by a boxcar integrator (Stanford Research Systems, SR 250).

All SH intensities are normalized to those obtained from the tensor element d_{11} of a half-wave plate of quartz in collinear geometry. Owing to its high degree of parallelity ($\lambda/20$), it provides a reproducible SH signal at perpendicular incidence, which does not necessarily correspond to a Maker fringe maximum. Furthermore, the intensities are divided by the crystal length L passed by the light. Thus we have

$$S_{ij} = (1/L)\, I(\mathrm{SH})_{ij}(\mathrm{SCT})/I(\mathrm{SH})(\mathrm{quartz}), \qquad (1)$$

corresponding to the calibration performed by Azzini *et al.*[13] The indices ij describe the directions of polarization of the detected SH light (i) and of the fundamental beam (j) with respect to the crystal axes lying in a plane perpendicular to $\mathbf{k}_\omega$.

III. EXPERIMENTAL RESULTS AND DISCUSSION

A. Measurements with $\mathbf{k}\|x$

Figure 3 shows the T dependences of the SHG intensities S_{yy} and S_{zz} recorded upon zero-field cooling and subsequent zero-field heating, with parallel polarizations of both the fundamental and SH beams in y and z direction, respectively. In both cases we measure a PT-like increase of the signal below $T_c\approx 18$ K, saturating at low temperatures $T\approx 5$ K. The temperature hysteresis of about 3 K can be explained by local pinning of polarization due to random fields.[5–7,14]

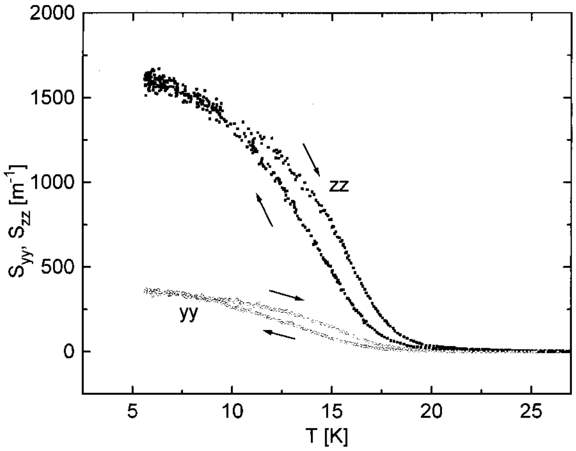

FIG. 3. Temperature dependences of the SH intensities S_{yy} and S_{zz} upon zero-field cooling and subsequent zero-field heating (arrows).

Surprisingly the SH intensity S_{zz} is nearly by a factor of 5 larger than S_{yy}, although the ferroelectric polarization of SCT only occurs along the easy axes x or y.[14] In both cases the corresponding SHG tensor of the symmetry group $2mm$ (x nanoregions) or $m2m$ (y nanoregions) reveals vanishing intensity S_{zz}.[10] This is sharply contradicted by the large SHG intensities occurring in this configuration. They demand for a novel mechanism of SHG to be discussed below.

This is supported by the measurements of the dependences on the polarization angle shown in Fig. 4. Here the polarization of the fundamental beam is rotated around the optical axis at fixed polarization, y or z, of the detected SH light. Note that the rotation angle of $\phi = 0$ corresponds to a y-polarized fundamental beam, whereas $\phi = \pm 90°$ correspond to a z-polarized fundamental beam. The measurements

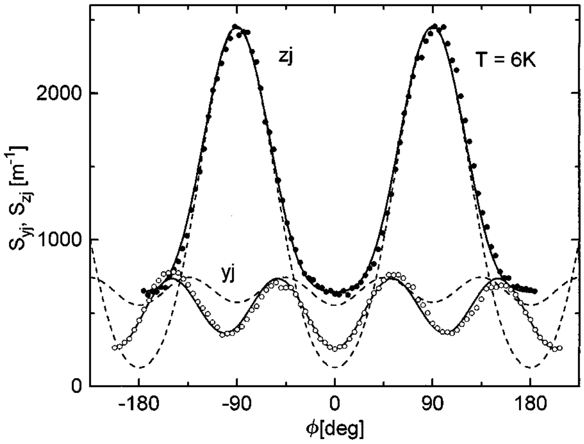

FIG. 4. Dependence of the y- (open circles) and z-polarized (solid circles) SH light intensities on the angle ϕ between the y axis and the polarization of the fundamental beam at $T = 6$ K. The solid lines represent best fits of Eqs. (2) and (3) to the data. The dashed lines refer to Eqs. (2) and (3) by using ratios of the coefficients listed in Table V for $a = 0.5$ and fitting to the respective peaks.

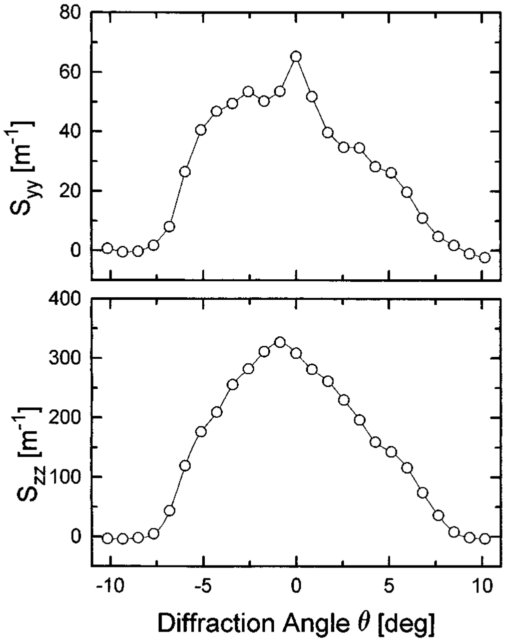

FIG. 5. Diffraction pattern (data points interpolated by splines) of the SHG intensities S_{yy} and S_{zz} in transmission geometry measured at $T=5.5$ K in zero external field (see text).

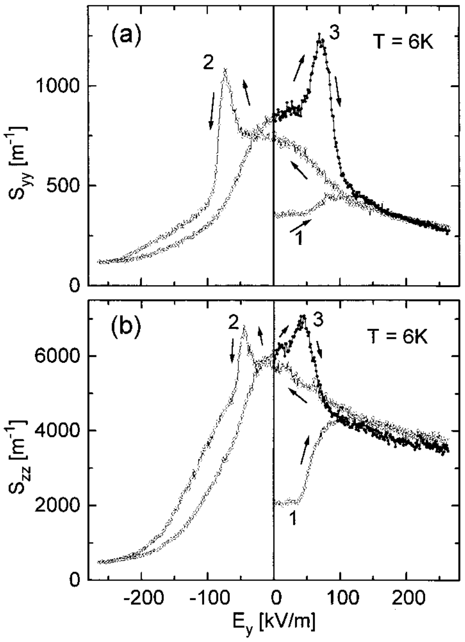

FIG. 6. Dependences of S_{yy} (a) and S_{zz} (b) on an external electric field E_y at $T=6$ K. The data connected by eye-guiding lines denoted by 1, 2, and 3 are successively recorded (see text).

are performed at $T=6$ K without an external electric field. It is seen that the y-polarized SH light S_{yj} reaches maximum intensity under $\phi=\pm 45°$ and $\phi=\pm 135°$ and, hence, under diagonal polarization of the fundamental beam. However, the intensity of z-polarized SH light S_{zj} becomes maximal at $\phi=\pm 90°$, which refers to a z-polarized fundamental beam. This contradicts expectation when assuming global C_{2V} symmetry. Just the contrary should occur at $\phi=\pm 90°$, viz., maximum yield for S_{yy} and vanishing efficiency for S_{zz}, since

$$S_{yj}(\phi)=c_1\cos^4\phi+c_2\cos^2\phi\sin^2\phi+c_3\sin^4\phi, \qquad (2)$$

$$S_{zj}(\phi)=c_4\cos^4\phi+c_5\cos^2\phi\sin^2\phi+c_6\sin^4\phi, \qquad (3)$$

where $c_1\propto d_{33}^2$, $c_2\propto 2d_{33}d_{15}$, $c_3\propto d_{15}^2$, $c_4=c_6=0$, $c_5 \propto 4d_{15}^2$. The tensor elements d_{ik} account for Kleinman's conditions[10] applied to C_{2V} symmetry under the assumption of equipartition of classes $m2m$ and $2mm$ (ac and $a'c$ nanoregions, respectively). Obviously c_2 is expected to interpolate between c_1 and c_3 for S_{yj}, whereas $c_5 \gg c_4, c_6$ should apply to S_{zj}. Best fitting the data to Eqs. (2) and (3), however, yields $c_1=260$, $c_2=2312$, and $c_3=364$ m^{-1}; hence, $c_2 \gg c_1, c_3$, and $c_4=644$, $c_5=1496$, and $c_6=2457$ m^{-1}; hence, $c_4<c_5<c_6$ (solid lines in Fig. 4). The ratios $c_1{:}c_2{:}c_3=0.11{:}1{:}0.16$ and $c_4{:}c_5{:}c_6=0.43{:}1{:}1.64$ are obviously incompatible with conventional symmetry considerations.

In order to resolve these contradictions, we consider that the SHG in SCT is due to the surfaces of ferroelectric nanoregions with a considerable shape anisotropy. Probably the ferroelectric nanoregions do not have spherical shapes, but are elongated along their respective polar axes as a consequence of the prolate shape of the Ca^{2+}-centered primary clusters (Fig. 1). In a model calculation given in detail in Sec. IV, an ellipsoidal nanoregion shape is assumed. Remarkably, the same types of angular dependences are found as described by Eqs. (2) and (3). Dominance of the cross term c_2 in the case of S_{yj} and of the $\sin^4$ term c_6 for S_{zj} supports our assumption of SHG at the surfaces of elongated ferroelectric nanoregions.

It should be remarked that our neglect of bulk contributions to SHG is corroborated by the fact that the total efficiency observed in SCT is relatively small. It is about one order of magnitude smaller than that observed, e.g., on a poled thin film of P(VDF-TrFE+10% PMMA with thickness 5 μm.[15] This seems to imply that either the bulk SHG tensor elements are anomalously small in SCT or that the size of the polar regions lies below the observability threshold as was discussed, e.g., in the case of glassy KTL.[16] Furthermore, we also believe that the SHG intensity cannot be due to the ferroelastic domain boundaries[2] shown in Fig. 1. Owing to their micrometric size, one easily estimates that their total wall area is about four order of magnitude smaller than that of the ferroelectric nanodomains. This seems to exclude a ferroelastic origin of SHG observed in SCT.

On the other hand, the intrinsic polar disorder is corroborated by an appreciable angular width of the SH light beam (Fig. 5). It is measured by moving a narrow slit in front of the collecting lens (Fig. 2) through the divergent SH beam parallel to the c axis of the sample. Both S_{yy} and S_{zz} are scattered around the sample normal at least up to angles $\Theta=\pm 10°$, which is our present aperture limit. Very probably this is primarily an effect of nonlinear diffraction[17] due to an ensemble of polar regions with randomly distributed size and polarity.[18] It remains to be shown that the observed diffraction pattern can be mapped onto the Poisson distribution of nanosize regions recently deduced for SCT with $x=0.002$ (Ref. 19) from the analysis of its dielectric dispersion. Following Ref. 18, we propose that the random array of

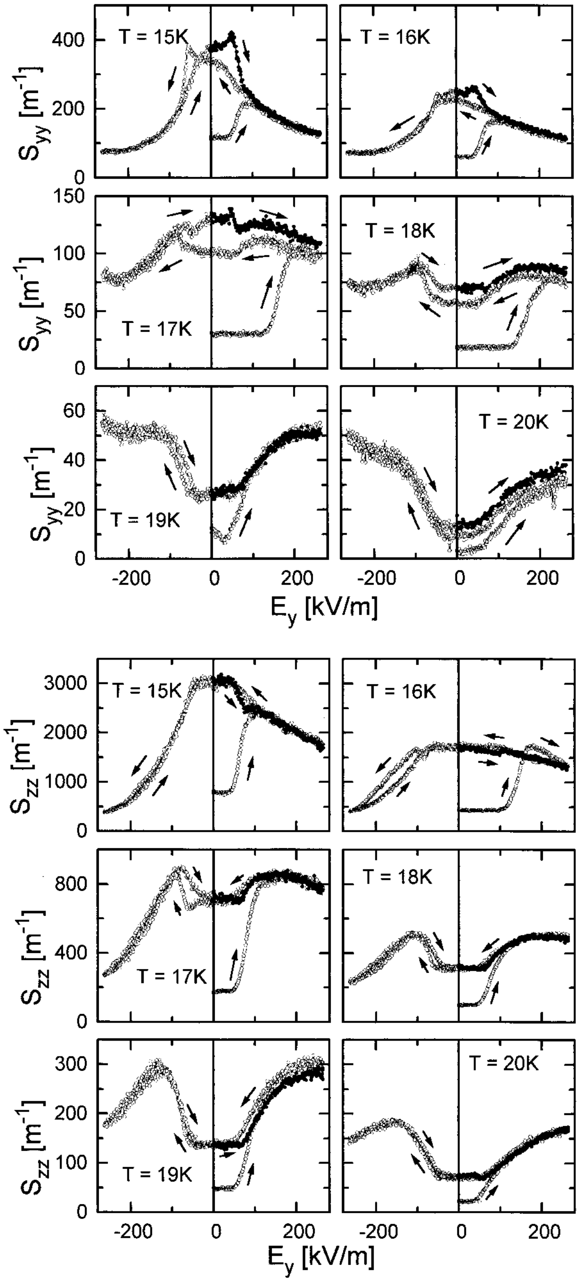

FIG. 7. Dependences of S_{yy} (a) and S_{zz} (b) on an external electric field E_y at $T = 15$, 16, 17, 18, 19, and 20 K recorded in the same way as indicated in Fig. 6.

polar nanoregions emits incoherent SH light, the angular distribution of which follows a slit function with maximum yield at $\Theta = 0$, in agreement with our experiment. Its width reflects that of the power spectrum corresponding to the "noise" signal of the size distribution.

Closer inspection of Fig. 5 shows distinct differences between S_{yy} and S_{zz}. Contrary to S_{zz}, asymmetric peaks at $\Theta \approx \pm 3°$ and a sharp maximum at $\Theta = 0$ are observed in S_{yy}. Presumably these are due to the periodic array of ferroelastic domains superimposed to the random nanoregion distribution. The asymmetry of the intensities seems to indicate near-Bragg diffraction[17] at a thick phase grating with a period of $\Lambda \approx 10$ μm in agreement with our observations under a polarizing microscope.[4] This diffraction phenomenon is due to the modulation of the refractive index (n_a and $n_{a'}$, respectively; see Fig. 1) probed by y-polarized light. It is absent in S_{zz} because of the essentially constant value of n_c along the orthorhombic c axis (Fig. 1).

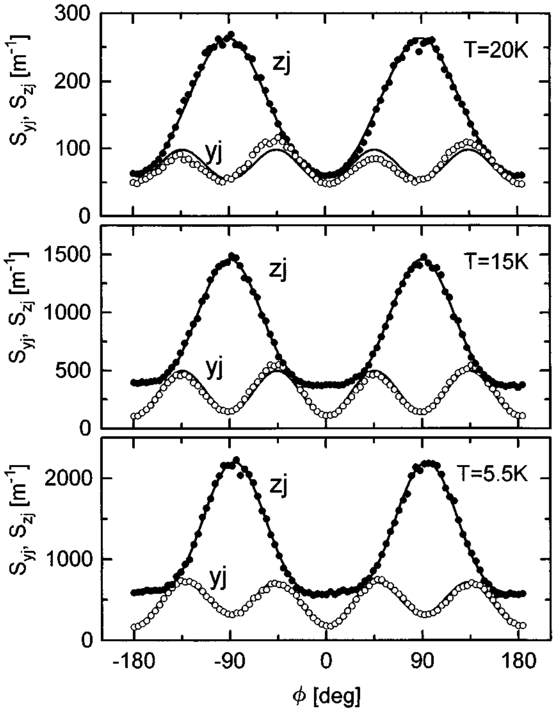

FIG. 8. Dependences of y- (open circles) and z-polarized (closed circles) SH light intensities on the angle ϕ between the y axis and the polarization of the fundamental beam at $T = 5.5$, 15, and 20 K with an external electric field $E_y = 263$ kV/m. The solid lines represent best fits of Eqs. (2) and (3) to the data.

In order to obtain further insight into the mechanisms of SHG in the SCT system, we measured S_{yy} and S_{zz} under the influence of an external field E_y. The results achieved at $T = 6$ K are shown in Fig. 6. In both cases the curves have qualitatively similar shapes. The virgin curves labeled as 1 first show an increase of the signal up to $E_y \approx 100$ kV/m followed by a decrease at higher fields. In particular, this decrease cannot be understood by assuming SHG within the bulk of ferroelectric nanoregions. Owing to the field-induced increase of ferroelectric coherence, at least the signal S_{yy} should increase at increasing fields. On the other hand, the behavior can again be understood by assuming surface SHG at ferroelectric nanoregions. Two consecutive processes must be taken into account. At low electrical fields nucleation of new ferroelectric nanoregions takes place, whereas condensation of the nanoregions occurs when they touch each other at higher fields. Nucleation of new nanoregions gives rise to an increasing number of surfaces and, hence, to an increase of the SHG signal. The subsequent condensation of nanoregions is connected with a decrease of the total area of the nanoregion surfaces and, hence, a decreasing signal.

After recording the virgin curves up to $E_Y = 260$ kV/m, the signals rise upon decreasing the electrical field and switching it into negative direction. Sharp peaks, denoted as 2, appear at $E_y = -75$ kV/m for S_{yy} and at $E_y = -50$ kV/m for S_{zz}, respectively. Obviously the field-induced process of condensation becomes inverted. While lowering the electri-

TABLE I. Best-fit parameters to Eqs. (2) and (3) of the dependences on the polarization angle of $S_{y/zj}$ shown in Fig. 8.

Curve	T (K)	$c_{1/4}$	$c_{2/5}$	$c_{3/6}$	$c_{1/4}:c_{2/5}:c_{3/6}$
S_{yj}	5.5	$c_1=182.8$	$c_2=2356$	$c_3=321.4$	0.07:1:0.14
S_{yj}	15	108.6	1741	142.2	0.06:1:0.08
S_{yj}	20	48.61	290.3	54.09	0.17:1:0.19
S_{zj}	5.5	$c_4=585.5$	$c_5=1077$	$c_6=2201$	0.54:1:2.04
S_{zj}	15	376.1	781.1	1460	0.48:1:1.87
S_{zj}	20	59.48	258.0	263.5	0.23:1:1.02

cal field, nucleation of ferroelectric nanoregions with polarization directed oppositely to the external field or of paraelectric regions occurs within the homogeneously polarized surrounding. This process has been interpreted[5–7] to be due to quenched local RF's characteristic of the SCT system. In zero field this process is not yet finished. Just after reaching the peaks at weak negative fields, a process of condensation of these new regions takes place, leading to a sudden decrease of the signal. After reaching minimal intensities, $S_{yy}\approx 120\ \mathrm{m}^{-1}$ and $S_{zz}\approx 500\ \mathrm{m}^{-1}$ at $E_y=-260$ kV/m, and subsequently increasing the field, the SH intensities increase again and reach new peaklike maxima (denoted as 3 in Fig. 6) at weakly positive values $E_y=70$ and 50 kV/m for S_{yy} and S_{zz}, respectively. Obviously the process of disintegration of condensed nanoregions and their most effective fine graining under weak inverted fields takes place similarly as in the preceding half-cycle.

The large SHG intensities observed after application of the external electric field hint at a finer nanoregion structure compared with that of the virgin state. In particular, this seems to characterize the nanoregion structure encountered at weakly negative fields, where S is peaking. It is noticed that both measurements shown in Fig. 6 are qualitatively similar, the crucial difference being their different amplitudes, viz., $S_{zz}\approx 5S_{yy}$. The shapes of the curves are obviously caused by the same processes, their quantitative difference being due to the anisotropic nanoregion shape (see Sec. IV).

The slight asymmetries observed in subsequent half-cycles and the occurrence of different peak heights 2 and 3, respectively, are not completely understood. They are fully reproducible when recording the virgin curves 1 within the second quadrant with $E_y<0$. Very probably, slight misorientation of the sample with respect to the crystallographic axes is at the origin of these asymmetries. They are also encountered in Fig. 7 (see below).

The dependences of the SHG intensities S_{yy} and S_{zz} measured at temperatures close to T_c between 15 and 20 K are shown in Figs. 7(a) and 7(b). At $T=15$ K for both configurations, the dependences on E_y resemble those obtained at $T=6$ K, the only differences being reductions by factors 2–2.5. However, at higher T we obtain new characteristics. At $T\geqslant 19$ K the curves S vs E_y become inverted. In the high-field range $|E_y|>100$ kV/m, the signals no longer decrease with increasing $|E_y|$, but increase until reaching saturation at $|E_y|\geqslant 200$ kV/m. This change of behavior might be caused by the following reason. The intrinsic nucleation of ferroelectric nanoregions is nearly negligible at this temperature (see Fig. 3). Hence nucleation continues under the influence of the electrical field without risking that the nanoregions touch each other and condensate owing to their smaller size at these temperatures. This means that even at high temperatures $T\approx T_c$, SHG is still determined by the surfaces of polar nanoregions. Since the total area of the surfaces is very small at high T, it might be argued that SHG then primarily arises in the volume of ferroelectric nanoregions or within paraelectric regions by virtue of field-induced polarization. However, again the ratio $S_{zz}/S_{yy}\approx 5$ contradicts this kind of interpretation. It should be noticed that the absolute SH effi-

TABLE II. Best-fit parameters to Eq. (4) of the relaxational behavior of S_{yy} shown in Fig. 9.

T (K)	c_0	c_1	c_2	τ_1 (s)	τ_2 (s)
Switching on					
6	186	−112	−25.8	18.9	579
8	170	−109	−23.6	11.5	351
10	157	−99	−21.2	10.4	403
12	125	−84	−14.4	7.8	387
14.4	71	−70	−12.9	4.5	101
Switching off					
6	147	25	4.3	15.1	508
8	131	16	19.1	3.5	30
10	115	27	3.6	11.2	261
12	80	30	8.6	8.7	298
14.4	42	24	1.8	4.7	155

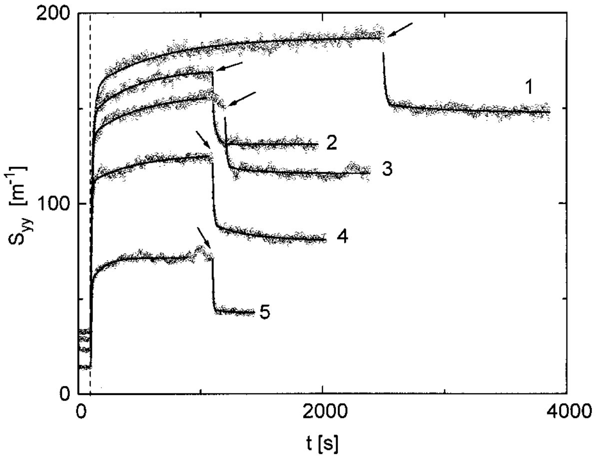

FIG. 9. Time dependences of S_{yy} upon switching on (dashed vertical line) and off (arrows) an external electric field $E_y=7.9$ kV/m after zero-field-cooling at $T=6$ K (curve 1), 8 K (2), 10 K (3), 12 K (4), and 14.4 K (5). The solid lines represent best fits of Eq. (4) to the data (see also Table II).

ciencies at $T=20$ K and $|E_y|=250$ kV/m are only by a factor of 3 smaller than those observed at the same field and $T=6$ K.

Another method to examine the origin of SHG at $T\approx T_c$ is to measure its dependence on the polarization angle under maximal electric field $E_y=263$ kV/m. In Fig. 8 we show results of measurements performed at $T=5.5$, 15, and 20 K. The resulting curves reveal qualitatively equal shapes at all T. Again, the SHG intensities S_{yj} are peaking at diagonal angles and S_{zj} becomes maximal at $\phi=\pm 90°$. In accordance with the model calculation in Sec. IV, this means that even at $T=20$ K and under a high electrical field SHG arises from surfaces of anisotropically shaped polar nanoregions. Similarly as in Fig. 4, the curves can be fitted to the functions given by Eqs. (2) and (3). The corresponding fit parameters are listed in Table I. The dominance of the cross term c_2 for S_{yj} and of the $\sin^4$ term c_6 for S_{zj} is obvious.

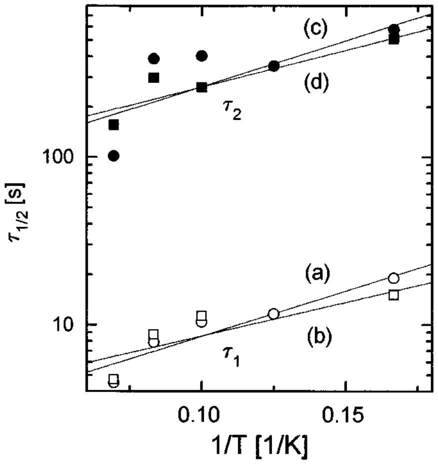

FIG. 10. Plots of the relaxation times τ_1 (a), (b) (open symbols) and τ_2 (c), (d) (solid symbols) vs $1/T$ obtained after switching on (a), (c) and off (b), (d) an external electric field (Fig. 9). The solid lines represent best fits to Arrhenius-type functions given by Eq. (5).

TABLE III. Best-fit parameters to Eq. (5) of the diagrams shown in Fig. 10.

	$\tau_{1\infty}$ (s)	$\tau_{2\infty}$ (s)	$\Delta E_1/k_B$ (K)	$\Delta E_2/k_B$ (K)
Switching on	2.46	75.1	12.4	12.6
Switching off	3.41	96.0	9.2	10.1

B. Measurements with k∥*z*

The measurements with $\mathbf{k}\|z$ are performed with a fundamental beam passing the sample along the z axis, the directions of polarization of both the fundamental and SH beams lying in the (xy) plane. We present results for the SHG intensity S_{yy}, where fundamental and SH beams are polarized along the y axis. In this configuration we examined the dynamics of the SHG signal while switching on and off an external electric field $E_y=7.9$ kV/m (Fig. 9). These measurements are performed at various temperatures $T=6$, 8, 10, 12, and 14.4 K, after zero-field cooling from $T\gg T_c$ in order to obtain identical initial states of the sample.

As expected, the initial value of S_{yy} after zero-field cooling decreases with increasing T, $S_{yy}\approx 30$ and 15 m^{-1} at $T=6$ and 14.4 K, respectively. After switching on the electrical field, a large enhancement of S_{yy} slowly occurs with saturation values $S_{yy}\approx 190$ m^{-1} at $T=6$ K to $S_{yy}\approx 70$ m^{-1} at $T=14.4$ K. When switching off at time t_0 (arrows in Fig. 9), the external field S_{yy} relaxes down to remanent values between 150 and 40 m^{-1} at $T=6$ and 14.4 K, respectively. The curves are fitted to double exponential functions of the type

$$S_{yy}=c_0+c_1\exp([t-t_0]/\tau_1)+c_2\exp([t-t_0]/\tau_2). \quad (4)$$

Similar relaxational behavior of SHG was found in the related system KTL.[20] The fitting parameters c_0, c_1, c_2, τ_1, and τ_2 are listed in Table II. We obtain short relaxation times τ_1 between 5 and 20 s and larger relaxation times τ_2 between 100 and 600 s (with the fortuitous exception of too small

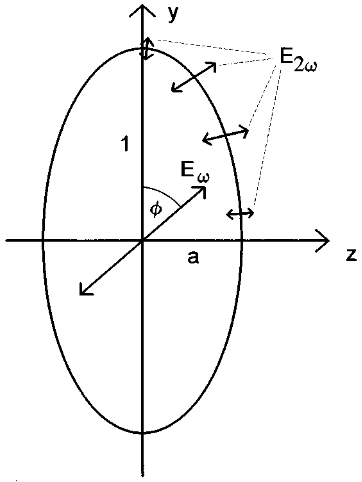

FIG. 11. Cross section of an ellipsoidally shaped nanoregion with the fundamental beam wave $\mathbf{E}_\omega$ under an angle ϕ with respect to the polar y axis and SH waves $\mathbf{E}_{2\omega}$ originating from the nanoregion surface.

values of τ_1 and τ_2 upon switching off the field at $T=8$ K; data are henceforth neglected).

The Arrhenius plots of $\log_{10}(\tau_j/s)$ vs $1/T$ in Fig. 10 seem to hint at thermally activated processes involved in the relaxation after both switching on [(a) and (c)] and off [(b) and (d)] the external field:

$$\tau_j=\tau_{j\infty}\exp(\Delta E_j/[k_B T]),\quad j=1,2. \tag{5}$$

The best-fit parameters $\tau_{j\infty}$ and ΔE_j are listed in Table III. They are connected with the dynamics of the polar nanoregions. Here we propose that the fast processes τ_1 and ΔE_1 refer to wall displacements, viz., nanoregion growth or shrinking under a steplike change of the external field. On the other hand, the slow processes τ_2 and ΔE_2 might refer to nucleation processes, which are more strongly hampered by the random field distribution than the wall displacements.

It should be stressed that the Arrhenius parameters obtained for the nanoregion dynamics amplitude largely decoupled from that of local hopping motion of the Ca^{2+} off-center dipoles. Their dynamics, as revealed by dielectric spectroscopy,[7] yields $\tau_\infty=1.4\times10^{-11}$ s and $\Delta E/k_B=175$ K. Compared with these values, the nanoregion walls are very sluggish, but rather soft. It should be stressed that the parameters listed in Table III are primarily determined by pinning forces due to dipolar random fields. Within this context it is interesting to notice that the dipolar switching times τ_1 and τ_2 observed in the present SHG experiment are at least two orders of magnitude larger than the quadrupolar switching times determined by the relaxation of field-induced birefringence.[12] Obviously the dipolar nanoregion rearrangement takes a longer time than the relaxation of the field-induced strain, being proportional to $\langle P_x^2\rangle$.

IV. MODEL CALCULATION OF INTERFACE SHG AT ANISOTROPIC POLAR NANOREGIONS

In order to model the observed peculiar angular dependences $S_{yj}(\phi)$ and $S_{zj}(\phi)$ (Figs. 4 and 8), we start from an isolated ellipsoidally shaped ferroelectric nanoregion embedded in the nonpolar host material. Figure 11 shows the cross section of a y-polarized nanoregion, the vector of the polarized fundamental beam, $\mathbf{E}_\omega$, and the SH field vector $\mathbf{E}_{2\omega}$ at several points on the nanoregion surface.

The ellipsoid intersects the y axis at ±1 and the x and z axes at the points $\pm a$ with $0<a\leqslant1$. SHG is assumed to arise only on the surface of the ellipsoid. In spherical coordinates the ellipsoid is described by

$$\mathbf{r}(\alpha,\beta)=(r_x,r_y,r_z)=(a\sin\alpha\,\cos\beta,\cos\alpha,a\sin\alpha\,\sin\beta), \tag{6}$$

with α and β the polar and the azimuthal angle to the y or x axis, respectively. The vector normal to the surface at $\mathbf{r}(\alpha,\beta)$ is given by

$$\begin{aligned}\mathbf{n}(\alpha,\beta)&=[(\partial\mathbf{r}/\partial\beta)\times(\partial\mathbf{r}/\partial\alpha)]/|[(\partial\mathbf{r}/\partial\beta)\times(\partial\mathbf{r}/\partial\alpha)]|\\&=(a\sin^2\alpha\,\cos\beta,a^2\sin\alpha\,\cos\alpha,a\sin^2\alpha\,\sin\beta)/(a^2\sin^4\alpha+a^4\sin^2\alpha\,\cos^2\alpha)^{1/2}.\end{aligned} \tag{7}$$

Maximum nonlinear surface polarizability is assumed to occur in the direction of $\mathbf{n}$. The absolute value of the SH amplitude $\mathbf{E}_{2\omega}$ is given by the squared projection of the fundamental beam amplitude $\mathbf{E}_\omega$ onto $\mathbf{n}$:

$$\mathbf{E}_{2\omega}(\alpha,\beta)=[\mathbf{E}_\omega\cdot\mathbf{n}(\alpha,\beta)]^2\mathbf{n}(\alpha,\beta), \tag{8}$$

where $\mathbf{E}_\omega/\mathbf{E}_\omega^0=(0,\cos\phi,\sin\phi)$.

Integration of $\mathbf{E}_{2\omega}$ over the surface of the ellipsoid would yield a vanishing result, since contributions from opposite sides of the ellipsoid cancel each other. For finite nanoregion sizes, however, this it not the case due to the phase mismatches of SH light from different spatial points. The true geometrical sizes of the nanoregions are not known and probably obey a percolation distribution function.[19] It suffices to know that each domain with finite thickness provides a vanishing contribution to the SHG intensity, since pairs of interfaces are successively hit by the fundamental wave with a finite phase shift. Obviously the coherence length encountered in ordinary bulk SHG is not relevant in the mechanism under consideration. Assuming a random spatial distribution of the nanoregions, decoupling of all partial SH waves can be conjectured. This is corroborated by the observation of incoherent scattering (Fig. 5). Hence a random-phase approximation seems appropriate, in which intensities are integrated instead of electrical fields. The integration is performed separately for the y and z contributions. We obtain

$$\begin{aligned}S_{yj}&\propto\oint\!\!\oint_F[E_{y,2\omega}(\alpha,\beta)]^2dF\\&=\int_{\alpha=0}^{\pi}\int_{\beta=0}^{2\pi}[E_{y,2\omega}(\alpha,\beta)]^2|(\partial\mathbf{r}/\partial\beta)\times(\partial\mathbf{r}/\partial\alpha)|d\beta\,d\alpha\\&=a^{12}\cos^4\phi\int_0^{\pi}\int_0^{2\pi}\frac{\sin^6\alpha\cos^6\alpha}{(a^2\sin^4\alpha+a^4\sin^2\alpha\,\cos^2\alpha)^{5/2}}d\beta\,d\alpha+6a^{10}\cos^2\phi\,\sin^2\phi\int_0^{\pi}\int_0^{2\pi}\frac{\sin^8\alpha\,\cos^4\alpha\,\sin^2\beta}{(a^2\sin^4\alpha+a^4\sin^2\alpha\,\cos^2\alpha)^{5/2}}d\beta\,d\alpha\\&\quad+a^8\sin^4\phi\int_0^{\pi}\int_0^{2\pi}\frac{\sin^{10}\alpha\,\cos^2\alpha\,\sin^4\beta}{(a^2\sin^4\alpha+a^4\sin^2\alpha\,\cos^2\alpha)^{5/2}}d\beta\,d\alpha\end{aligned} \tag{9}$$

and

$$
\begin{aligned}
S_{zj} &\propto \oiint_F [E_{z,2\omega}(\alpha,\beta)]^2 dF \\
&= \int_{\alpha=0}^{\pi}\int_{\beta=0}^{2\pi} [E_{z,2\omega}(\alpha,\beta)]^2 |(\partial \mathbf{r}/\partial\beta)\times(\partial\mathbf{r}/\partial\alpha)| d\beta\, d\alpha \\
&= a^{10}\cos^4\phi \int_0^{\pi}\int_0^{2\pi} \frac{\sin^8\alpha\,\cos^4\alpha\,\sin^2\beta}{(a^2\sin^4\alpha + a^4\sin^2\alpha\,\cos^2\alpha)^{5/2}} d\beta\, d\alpha + 6a^8\cos^2\phi\,\sin^2\phi \int_0^{\pi}\int_0^{2\pi} \frac{\sin^{10}\alpha\,\cos^2\alpha\,\sin^4\beta}{(a^2\sin^4\alpha + a^4\sin^2\alpha\,\cos^2\alpha)^{5/2}} d\beta\, d\alpha \\
&\quad + a^6\sin^4\phi \int_0^{\pi}\int_0^{2\pi} \frac{\sin^{12}\alpha\,\sin^6\beta}{(a^2\sin^4\alpha + a^4\sin^2\alpha\,\cos^2\alpha)^{5/2}} d\beta\, d\alpha .
\end{aligned}
\qquad (10)
$$

Equations (9) and (10) reveal exactly the same angular dependences as Eqs. (2) and (3) in Sec. III. The integrals given in Eqs. (9) and (10) can be solved numerically. Some results are listed in Table IV for various values of a. In order to compare with the measured values of the ratio $c_{1/4}:c_{2/5}:c_{3/6}$ for $S_{yj/zj}$ (Table I), we also list these values as calculated for various choices of a in Table V. Inspection shows that reasonable agreement with the experimental data (except for the depth of the minima) is obtained for $a\approx 0.5$ (Fig. 4, dashed lines). This value provides dominance of c_2 for S_{yj} and of c_6 for S_{zj} similarly as observed experimentally.

The agreement with the experimental data would certainly be improved by taking into account a finite distribution of ellipticities, $1/a$. E.g., in our calculation those nanoregions with the polar axis in the x direction are not taken into account. They should contribute as ellipsoids with $a=1$. Furthermore, in a more rigorous treatment, the assumption of ellipsoidal domain shapes has to be abandoned. The real shape is probably much more complex (cf. Fig. 1). Considering about 30–300 (Ref. 7) ferroelectrically coupled Ca^{2+}-centered clusters under the constraint of quenched dipolar RF's, nonellipsoidal nanoregion shapes are highly probable. In particular, surface roughness of the nanoregions has to be taken into account. More realistic models of the nanoregion morphology would also allow one to overcome the random-phase approximation. It might eventually be replaced by correctly integrating the SH field vectors and their phases over the nanoregion surfaces.

Despite these obvious deficiencies, the basic assumption of our ansatz, namely, the neglect of bulk SHG, seems appropriate. In particular, this is corroborated by the observation of virtually no change of the angular dependences $S_{yj/zj}$ vs ϕ at high temperatures $T\approx T_c$ and in strong electrical fields. This clearly hints at interface SHG of small ferroelectric nanoregions embedded in a paraelectric surrounding.

V. CONCLUSION

The essential result of this study is that SHG in $\mathrm{Sr}_{1-x}\mathrm{Ca}_x\mathrm{TiO}_3$, $x=0.007$, is determined by the interfaces between ferroelectric nanoregions and their paraelectric surrounding. Volume SHG within the nanoregions seems to be negligible. To the best of our knowledge, such a behavior has never been observed in other systems. It sheds light onto the very peculiar nanoregion structure of the SCT system. Owing to the percolative nature of its ferroelectric PT,[7,12] the total area of internal interfaces is extremely large, thus enhancing the probability of dominant interface SHG. It will be interesting to check also other impurity systems undergoing structural PT's, but preserving dipolar disorder. We propose that $\mathrm{KTa}_{1-x}\mathrm{Nb}_x\mathrm{O}_3$ with $x=0.017$ might be another candidate[21] revealing interface-dominated SHG.

Measurements of the dependences of the SH intensities on an external electric field and on the direction of the fundamental wave polarization are in agreement with our hypothesis. In order to explain the angular dependences, a model calculation is given, which roughly confirms the experimental observations. This calculation is valid within the random-phase approximation. It becomes invalid above T_c, where the nanodomains decay into Ca^{2+}-centered polar clusters with sizes of only a few angstroms. In fact, no SHG is ob-

TABLE IV. Numerical values of the integrals in Eqs. (9) and (10).

	$a=1$	$a=0.5$	$a=0.05$	$a=0.005$
$\int_0^{\pi}\int_0^{2\pi}\frac{\sin^6\alpha\cos^6\alpha}{(\cdots)^{5/2}}d\beta\, d\alpha$	1.795	736.8	1.067×10^{11}	1.072×10^{19}
$\int_0^{\pi}\int_0^{2\pi}\frac{\sin^8\alpha\cos^4\alpha\sin^2\beta}{(\cdots)^{5/2}}d\beta\, d\alpha$	0.3590	63.82	2.259×10^{8}	2.634×10^{14}
$\int_0^{\pi}\int_0^{2\pi}\frac{\sin^{10}\alpha\,\cos^2\alpha\sin^4\beta}{(\cdots)^{5/2}}d\beta\, d\alpha$	0.3590	30.10	1.004×10^{7}	1.166×10^{12}
$\int_0^{\pi}\int_0^{2\pi}\frac{\sin^{12}\alpha\,\sin^6\beta}{(\cdots)^{5/2}}d\beta\, d\alpha$	1.795	77.51	9.815×10^{6}	9.869×10^{11}

TABLE V. Calculated intensity ratios according to Eqs. (2) and (3) for y- and z-polarized SH intensities.

	$c_1:c_2:c_3$	$c_4:c_5c_6$
$a=1$	0.83:1:0.17	0.17:1:0.83
$a=0.5$	0.48:1:0.31	8.8×10^{-2}:1:1.70
$a=0.05$	0.20:1:2.96	9.3×10^{-3}:1:65
$a=0.005$	0.17:1:29.5	9.4×10^{-4}:1:5.6×10^{3}

served in that temperature range. Only after undergoing the PT below $T_c\approx18$ K does the average cluster size increase by orders of magnitude[6] and SHG occur as a consequence of finite phase shifts across the cluster diameters. Field-induced enhancement of SHG due to ‘‘nucleation’’ can be understood in a similar way.

Relaxation measurements reveal Arrhenius-activated behavior of slow domain wall dynamics under the constraint of dipolar random fields. It will be interesting to compare details of this extremely slow dynamics with predictions for the domain wall response in the presence of RF pinning.[22]

ACKNOWLEDGMENT

This work was supported by the Deutsche Forschungsgemeinschaft within the Schwerpunktprogramm ‘‘Pseudosymmetrische Kristalle.’’

---

[1] W. Prusseit-Elffroth and F. Schwabl, Appl. Phys. A **51**, 361 (1990).

[2] T. Bleser, B. Berge, U. Bismayer, and E. K. H. Salje, J. Phys. Condens. Matter **6**, 2093 (1994).

[3] Y. R. Shen, Nature **337**, 519 (1989).

[4] U. Bianchi, W. Kleemann, and J. G. Bednorz, Ferroelectrics **157**, 165 (1994).

[5] W. Kleemann, F. J. Schäfer, K. A. Müller, and J. G. Bednorz, Ferroelectrics **80**, 297 (1988).

[6] U. Bianchi, W. Kleemann, and J. G. Bednorz, J. Phys. Condens. Matter **6**, 1229 (1994).

[7] U. Bianchi, J. Dec, W. Kleemann, and J. G. Bednorz, Phys. Rev. B **51**, 15 188 (1995).

[8] H. Uwe, H. Yamaguchi, and T. Sukudo, Ferroelectrics **96**, 123 (1989).

[9] M. G. Stachiotti and R. L. Migoni, J. Phys. Condens. Matter **2**, 4341 (1990).

[10] R. Bechmann, R. F. S. Hearmon, and S. K. Kurtz, in *Condensed Matter*, edited by K.-H. Hellwege and A. M. Hellwege, Landolt-Börnstein, New Series, Group III, Vol. 2 (Springer, Berlin, 1969).

[11] C. W. van Hasselt, M. A. Verheijen, and Th. Rasing, Phys. Rev. B **42**, 9263 (1990).

[12] W. Kleemann, U. Bianchi, A. Bürgel, M. Prasse, and J. Dec, Phase Transit. (to be published).

[13] G. A. Azzini, G. P. Banfi, E. Giulotto, and U. T. Höchli, Phys. Rev. B **43**, 7473 (1991).

[14] J. G. Bednorz and K. A. Müller, Phys. Rev. Lett. **52**, 2289 (1984).

[15] A. Bürgel, W. Kleemann, M. Biebricher, and H. Franke, Appl. Phys. A **60**, 475 (1995).

[16] G. P. Banfi and N. Samoggia, Nuovo Cimento **10**, 453 (1988).

[17] I. Freund, Phys. Rev. Lett. **21**, 1404 (1968).

[18] I. Freund, M. Deutsch, and A. Sprecher, Biophys. J. **50**, 693 (1986).

[19] W. Kleemann, A. Albertini, R. V. Chamberlin, and J. G. Bednorz (unpublished).

[20] P. Voigt and S. Kapphan, Ferroelectrics **157**, 239 (1994).

[21] A. Klössner, U. A. Leitão, W. Kleemann, and D. Rytz, Ferroelectrics **157**, 245 (1994).

[22] T. Nattermann, Y. Shapir, and I. Vilfan, Phys. Rev. B **42**, 8577 (1990).